Critical angle of reflections and Poisson's ratio from spectral recomposition

Zuniga, Nelson Ricardo Coelho Flores; Draganov, Deyan; Ghose, Ranajit

DOI
10.1016/j.jappgeo.2023.105110

Publication date
2023

Document Version
Final published version

Published in
Journal of Applied Geophysics

Journal of Applied Geophysics 215 (2023) 105110

Contents lists available at ScienceDirect

Journal of Applied Geophysics

journal homepage: www.elsevier.com/locate/jappgeo

Critical angle of reflections and Poisson's ratio from spectral recomposition

Nelson Ricardo Coelho Flores Zuniga [a,b,*], Deyan Draganov [c], Ranajit Ghose [c]

[a] Instituto de Astronomia, Geofísica e Ciências Atmosféricas da Universidade de São Paulo (IAG-USP), Rua do Matão 1226 - Cidade Universitária, – 05508-090, Department of Geophysics, São Paulo, SP, Brazil

[b] Escola Politécnica da Universidade de São Paulo (POLI-USP), Department of Mining and Petroleum Engineering, Avenida Pro. Luciano Gualberto 380, Cidade Universitária, São Paulo 05508-010, SP, Brazil

[c] Faculty of Civil Engineering and Geosciences, Delft University of Technology, Stevinweg 1, 2628 CN Delft, the Netherlands

ARTICLE INFO

Keywords:
Critical angle
Poisson's ratio
Spectral recomposition
Inversion
Frequency spectrum

ABSTRACT

Using the critical angle information of a reflection event, it is possible to calculate several essential physical parameters that are key to reliable geological characterization of the subsurface. However, estimation of the critical angle usually requires several steps of seismic processing. For this reason, an approach which is capable of estimating the critical angle directly from the data is of interest. Once the critical angle is estimated, it is possible to estimate further the Poisson's ratio and the seismic velocities. In this work, we propose an approach which can perform this estimation, based on spectral recomposition of seismic data. We design an inversion scheme in order to reconstruct the seismic spectrum of wavelets of a reflection event, which subsequently allows us to estimate the critical angle of near-surface reflection events without performing prior velocity analysis. After finding the critical angle, we show next how to estimate the Poisson's ratio and the compressional- and shear-wave velocities of the medium above the reflector. The approach leads to quite accurate values for Poisson's ratio even for noisy data, in case the number of layers is not large.

1. Introduction

The critical angle (CA) of a seismic reflection event at a subsurface boundary is an important piece of information in performing analyses of a seismic dataset. In comparison to deeper targets, in near-surface reflection measurements, CAs are quickly reached at shorter offsets due to sharp changes in the velocities with depth. Post-critical reflections are usually treated uniquely as informative events. To obtain a stacked image with a high signal-to-noise ratio (SNR), the position of the CA should be considered during the stacking process. Information about the CA is usually obtained from the Snell's law applied to the estimated velocities (Roth et al., 1998; Zelt et al., 2013), which demands a reliable prior estimate of the compressional (P) and/or shear (S) wave velocities. Uncertainties in the estimated velocities above and below an interface would result in uncertainties in the estimated CA. Because of this, it is desirable to have an alternative method that does not require prior velocity estimation, but uses the recorded reflections themselves to estimate the CA.

Spectral recomposition is a technique that can be used to extract useful information from a seismic spectrum (Tomasso et al., 2010; Li et al., 2011; Cai et al., 2013). It is usually performed by estimating the fundamental signal properties, such as peak frequency, amplitude and phase, in order to reconstruct the seismic spectrum (Castagna et al., 2003; Tomasso et al., 2010; Cai et al., 2013). One can reconstruct a seismic spectrum automatically by an inversion procedure if there is a mathematical description of the analyzed wavelet, which would allow performing the inversion for recovering the above-mentioned signal properties.

The phase of a reflected wave changes sharply when the CA is reached. Because in case of near-surface reflectors the CA is reached at relatively short offsets, the number of pre-critical traces to perform common-midpoint stacking is often limited (Roth et al., 1998; Zelt et al., 2013; Purves, 2014; Paskvich, 2016). This makes it more difficult to estimate reliable RMS velocities through velocity analysis, and consequently, harder to estimate also the Poisson's ratio. For this reason, an approach which allows obtaining directly from data the Poisson's ratio and the seismic wave velocities by finding the CA of a reflection event is of interest.

We develop an inversion approach to reconstruct the seismic spectrum of a reflection event and subsequently to estimate the CA. To do

* Corresponding author at: Instituto de Astronomia, Geofísica e Ciências Atmosféricas da Universidade de São Paulo (IAG-USP), Rua do Matão 1226 - Cidade Universitária, São Paulo, SP 05508-090, Brazil.

E-mail addresses: nelson.zuniga@iag.usp.br (N.R.C.F. Zuniga), D.S.Draganov@tudelft.nl (D. Draganov), R.Ghose@tudelft.nl (R. Ghose).

https://doi.org/10.1016/j.jappgeo.2023.105110
Received 23 January 2023; Received in revised form 2 May 2023; Accepted 11 June 2023
Available online 14 June 2023

this, we fit a calculated spectrum to an observed one, where the calculated curve is the mathematical representation of a Ricker wavelet (Ricker, 1953) and the observed curve is the wavelet of a reflection event in a recorded trace. Curve fitting is performed for each wavelet along a reflection event in a common source gather. In this way, it is possible to observe the anomalies after the inversion for each wavelet, and therefore, to identify the anomalies related to the CA of that reflection event. Contrary to conventional approaches which estimate Poisson's ratio directly from the elastic indentation of the material (Choi and Zheng, 2006; Zheng et al., 2009) or from P- and S-wave velocities through velocity analysis (Nishimura et al., 1960; Law et al., 1995; Bachrach et al., 2000; Zhang and Bentley, 2005; Raharjo et al., 2016; Yu et al., 2016), our approach allows obtaining the CA of a reflection event directly from the data, without the need to perform the velocity analysis. Once the CA is obtained, we can then calculate the Poisson's ratio and the P- and S-wave velocities of the layers.

It is important to note that the approach that we propose here does not require relatively long offsets (e.g., Landro and Tsvankin, 2007), or transforming the data to other domains, such as the τ-p domain (e.g., Sil and Sen, 2009). Our approach demands sufficient minimum number of offsets so we would be able to identify a decrease in the value of the global minima (i.e., only few offsets beyond the CA). CAs are seen in a τ-p section as blobs of increased amplitude. Even though the τ-p domain allows using shorter offsets compared to the method of Landro and Tsvankin (2007), the needed offset is still considerable. Also, data in the τ-p domain is often affected by transform artefacts, and other techniques are needed to reduce/suppress these artefacts (Dunne and Beresford, 1995). As a result, the selection of the most appropriate τ-p transform method is data-dependent. Furthermore, analysis in the τ-p domain provides the critical slowness. One needs the accurate velocity information in the upper layer in order to obtain CA from the critical slowness. In comparison, the method that we propose in this paper does not require a priori conventional velocity information for estimating the Poisson's ratio; it requires information obtained in the field, such as the depth of the first interface or the P-wave velocity top layer estimated, for example, from the direct wave. However, for estimating the velocities of the underlaying layers it still requires the P-wave velocity of the top layer. The proposed method works on a trace-by-trace basis, which allows stopping the analysis at offsets shortly after the CA. This renders this approach suitable for datasets having limited source-receiver offsets, unlike other methods that require larger offsets.

2. Theory

2.1. Spectral recomposition

The amplitude and phase spectrum of a seismic trace can be represented as a sum of different Ricker-wavelets amplitude and phase spectra, as proposed by Tomasso et al. (2010):

$$d(f) \approx \sum_{i=1}^{n} a_i \psi_i(m_i, f), \tag{1}$$

where $d(f)$ is the amplitude and phase spectrum of a seismic trace, f is frequency, and a_i and m_i are the amplitude and the peak frequency of the i-th Ricker-wavelet spectrum, respectively. A Ricker-wavelet amplitude and phase spectrum with a peak frequency at m is given by

$$R(f) = a\psi(m,f) = a\frac{f^2}{m^2} exp\left(-\frac{f^2}{m^2}\right). \tag{2}$$

Spectral recomposition can be used to obtain the peak frequency and the amplitude from a amplitude and phase spectrum through reconstruction. This differs from other approaches which decompose the amplitude and phase spectrum (Huang et al., 1998; Castagna et al., 2003; Li et al., 2011; Cai et al., 2013).

Using the above mathematical description for the amplitude and phase spectrum of a Ricker wavelet, it is possible to treat the problem in an inverse manner aiming to fit a calculated amplitude and phase spectrum to the one obtained from an observed wavelet in each seismic trace. The objective function to be used is shown in the Appendix. This allows us to recover the parameters related to the key components, i.e., peak frequency and amplitude, from the spectrum, and hence, analyze the residual error for each wavelet of a seismic reflection event.

2.2. Critical angle (CA) and Poisson's ratio

The CA of a PP reflected event (incident and reflected P waves) can be described by the Snell's Law as

$$\frac{sin(\alpha_c)_{P_1P_2}}{V_{P_1}} = \frac{sin(90^\circ)}{V_{P_2}}, \tag{3}$$

where α_c is the CA between the first and the second layer, while V_{P_1} and V_{P_2} are the P-wave velocities of the first and the second layer, respectively.

Rearranging eq. 3, we get:

$$sin(\alpha_c)_{P_1P_2} = \frac{V_{P_1}}{V_{P_2}}. \tag{4}$$

The same relation can also be written for an SS reflection event (incident and reflected S wave):

$$\frac{sin(\alpha_c)_{S_1S_2}}{V_{S_1}} = \frac{sin(90^\circ)}{V_{S_2}}, \tag{5}$$

where V_{S_1} and V_{S_2} are the S-wave velocities of the first and the second layer, respectively.

Rearranging eq. 5, we get:

$$sin(\alpha_c)_{S_1S_2} = \frac{V_{S_1}}{V_{S_2}}. \tag{6}$$

For the converted SP reflected event (incident S-wave and reflected P-wave), the relation is

$$\frac{sin(\alpha_c)_{S_1P_2}}{V_{S_1}} = \frac{sin(90^\circ)}{V_{P_2}}. \tag{7}$$

Rearranging eq. 7, we get:

$$sin(\alpha_c)_{S_1P_2} = \frac{V_{S_1}}{V_{P_2}}. \tag{8}$$

Dividing eq. 6 by eq. 8 results in

$$\frac{sin(\alpha_c)_{S_1S_2}}{sin(\alpha_c)_{S_1P_2}} = \frac{\frac{V_{S_1}}{V_{S_2}}}{\frac{V_{S_1}}{V_{P_2}}} = \frac{V_{P_2}}{V_{S_2}}. \tag{9}$$

Similarly, dividing eq. 8 by eq. 4 results in

$$\frac{sin(\alpha_c)_{P_1P_2}}{sin(\alpha_c)_{S_1P_2}} = \frac{\frac{V_{P_1}}{V_{P_2}}}{\frac{V_{S_1}}{V_{P_2}}} = \frac{V_{P_1}}{V_{S_1}}. \tag{10}$$

Therefore, the ratio of the CA of the SS and SP reflected events gives the ratio V_{P_1}/V_{S_1} of the first layer, while the ratio of the CA of the PP and SP reflected events leads to the ratio V_{P_2}/V_{S_2} of the second layer.

Since the Poisson's ratio can be expressed as

$$v = \frac{\left(\frac{V_P}{V_S}\right)^2 - 2}{2\left(\frac{V_P}{V_S}\right)^2 - 2}, \tag{11}$$

assuming the layers to be locally homogeneous and isotropic for the offsets in the common source gather, the Poison's ratio of the first (upper) layer can be written as

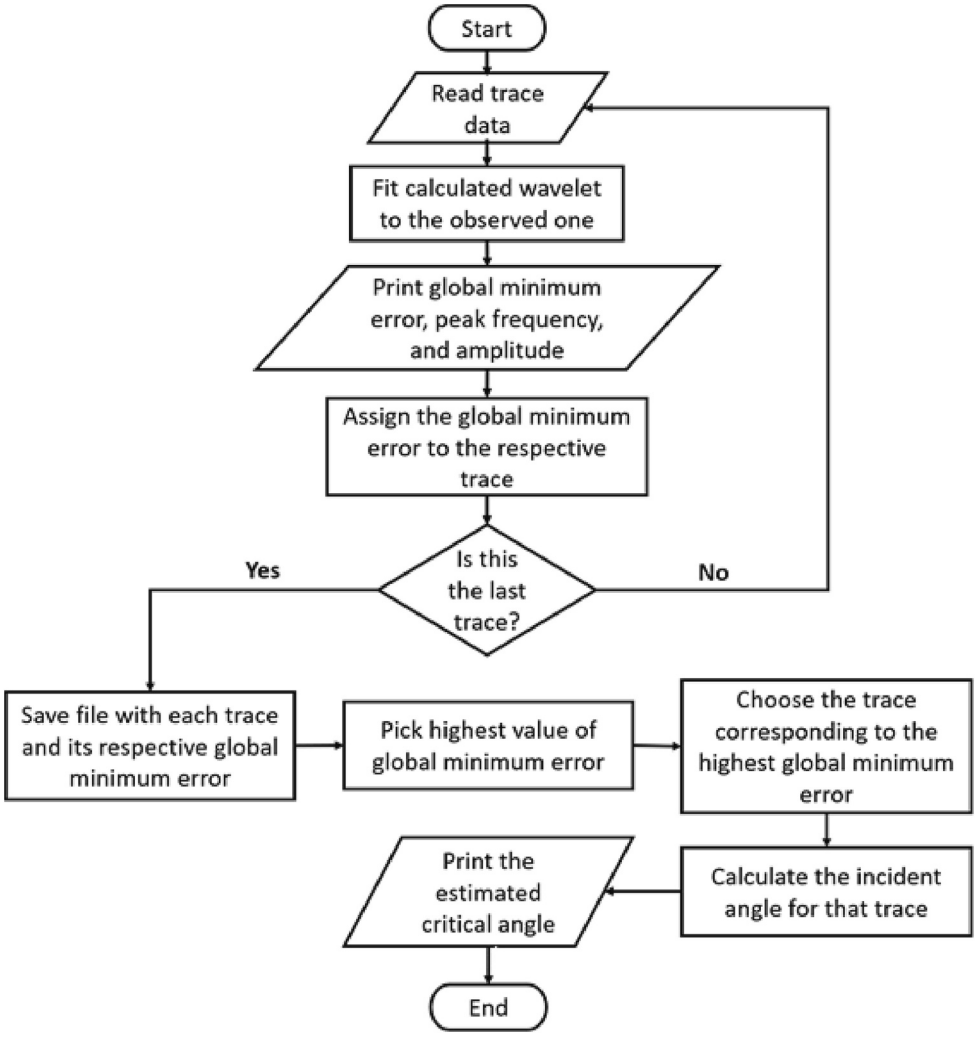

Fig. 1. Flowchart of the proposed algorithm.

$$v_1 = \frac{\left(\frac{\sin(\alpha_c)_{P_1P_2}}{\sin(\alpha_c)_{S_1P_2}}\right)^2 - 2}{2\left(\frac{\sin(\alpha_c)_{P_1P_2}}{\sin(\alpha_c)_{S_1P_2}}\right)^2 - 2}, \tag{12}$$

while for the second (lower) layer the Poisson ratio is

$$v_2 = \frac{\left(\frac{\sin(\alpha_c)_{S_1S_2}}{\sin(\alpha_c)_{S_1P_2}}\right)^2 - 2}{2\left(\frac{\sin(\alpha_c)_{S_1S_2}}{\sin(\alpha_c)_{S_1P_2}}\right)^2 - 2}. \tag{13}$$

Therefore, finding the CAs of the three reflected events would in principle allow obtaining the Poisson's ratio of the first two layers, without any prior information of the P- and S-wave velocities.

The same approach can be applied to the next layer, once the CA is found for the following (lower) interface. With the CAs of the PP, SS and SP events reflected at the interface between the second and the third layer, it is possible to find the Poisson's ratio for the third layer. This process can be continued successively for the deeper layers, as long as the recorded data contain the critically reflected arrivals. For noisy datasets, one needs to be careful to apply this method, as the error propagates from one layer to another during the recursion.

2.3. Calculating velocities from the CA

Using eqs. 4, 6, and 8, it is also possible to obtain V_P and V_S of both layers. For this, P-wave velocity V_{P_1} of the first layer will need to be estimated, which could be achieved by any other conventional method. Once V_{P_1} is estimated, it can be used in eq. 4 to calculate V_{P_2}.

Applying the same approach to eq. 8 would allow calculation of V_{S_2}. Next, substituting the calculated V_{S_2} in eq. 6, V_{S_1} can be found.

Thus, once the CAs of the PP, SS, and SP events, and the P-wave velocity of the first layer are estimated, it is possible to calculate the S-wave velocities of both layers and the P-wave velocity of the second layer.

3. Algorithm

3.1. Finding the CA

With the mathematical description presented in eqs. 1 and 2, it is possible to calculate the amplitude and phase spectrum of the Ricker-wavelet. After time-windowing a reflection event in an observed trace (which we call “observed wavelet”) and transforming it to the frequency domain, it is possible to fit a spectrum calculated from eqs. 1 and 2 to that of the observed one.

We have developed an inversion scheme, where the optimization is performed through curve fitting. Since the Ricker-wavelet spectrum is an observed quantity (i.e., it can be obtained from the observed data), the parameters to be recovered with the inversion are the peak frequency m and the amplitude a (see eqs. 1 and 2).

Instead of using global-search algorithms, we apply a multi-start procedure which employs a local-search routine (Terlaky and Sotirov, 2010). From random starting points, after several iterations, the approach leads to a good statistical distribution of the minima region. We perform least-square minimization of the difference between the Ricker-wavelet spectrum of the observed trace and the theoretical spectrum obtained from eqs. 1 and 2. In the stochastic process, each iteration results in a different minimum value, which can then be compared with the minima from other iterations. It is possible to select finally the largest minimum value. The number of iterations can be set to adapt to the complexity of the analyzed spectra, increasing the accuracy and the efficiency of recovering m and a corresponding to the global minimum region.

This mapping also provides a deeper understanding of the complexity of the topology of this objective function, allowing – if necessary - an improved inversion through selection of a more appropriate optimization algorithm and/or minimization method.

For an analyzed reflection event, this inversion is applied to each trace that contains this event, resulting in a set of peak frequencies and amplitudes. Also, each optimum set of parameters (m and a) recovered for each trace presents a residual error value. This residual error, related to the global-minimum region, can be used to identify the trace that contains the reflection arrival at the CA. For the trace at the CA, the residual corresponding to the global minimum is highest when compared with the same for the other traces. This is because at the CA the separation between the reflected wavelet and the critically refracted wavelet reaches the maximum value. Note that, our proposed procedure allows identifying the CA without the need of obtaining the velocities first. Note that the highest global minimum is related to trace number which is closest to the CA, and not to the CA itself; so, we can convert the trace number to angle, information obtained in the field is required, for example, the depth of the first interface or the P-wave velocity top layer estimated by direct wave.

The flowchart of the proposed algorithm is presented in Fig. 1.

3.2. Finding the Poisson's ratio

Estimating the CAs for different reflected wave types at a given interface allows us to find next the Poisson's ratio. For this purpose, the necessary events are the conventional PP reflection, the SvSv or ShSh reflection, and the converted SvP reflection. As the PSv and SvP reflections have the same arrival times (i.e., these two reflection events overlay each other), the CA of the SvP reflection appears sooner than the CA of the PSv reflection, which makes the estimation of the CA of the PSv reflection event more ambiguous when using our method. This ambiguity becomes even stronger in case of noisy data, which would prevent the use of PSv reflection event in most cases. For this reason, instead of PSv events, the use of SvP reflections is preferred. In this vein, we can restrict ourselves to specific areas of the seismogram in order to pick the target reflections. This prevents the algorithm from picking the wrong spectrum.

In practical implementation, one can carefully mute parts of the seismogram that are not of interest. This minimizes greatly the number of wavelets to be inverted, hence reducing the processing time and increasing the accuracy. In case a part of a target reflection event is inadvertently muted, that will result in an erroneous result.

When only single-component seismic data are available, identification of the three required wave types is not possible. We can still use the proposed approach to identify the CAs, which can subsequently be used to improve the NMO (normal moveout) stacking and hence enhance the signal-to-noise ratio of the stacked image. Furthermore, instead of conventional reflection shooting, a properly tailored, limited-offset, two-component reflection survey can be both economic and advantageous for estimating the CA, the Poisson's ratios, and the velocities using our approach.

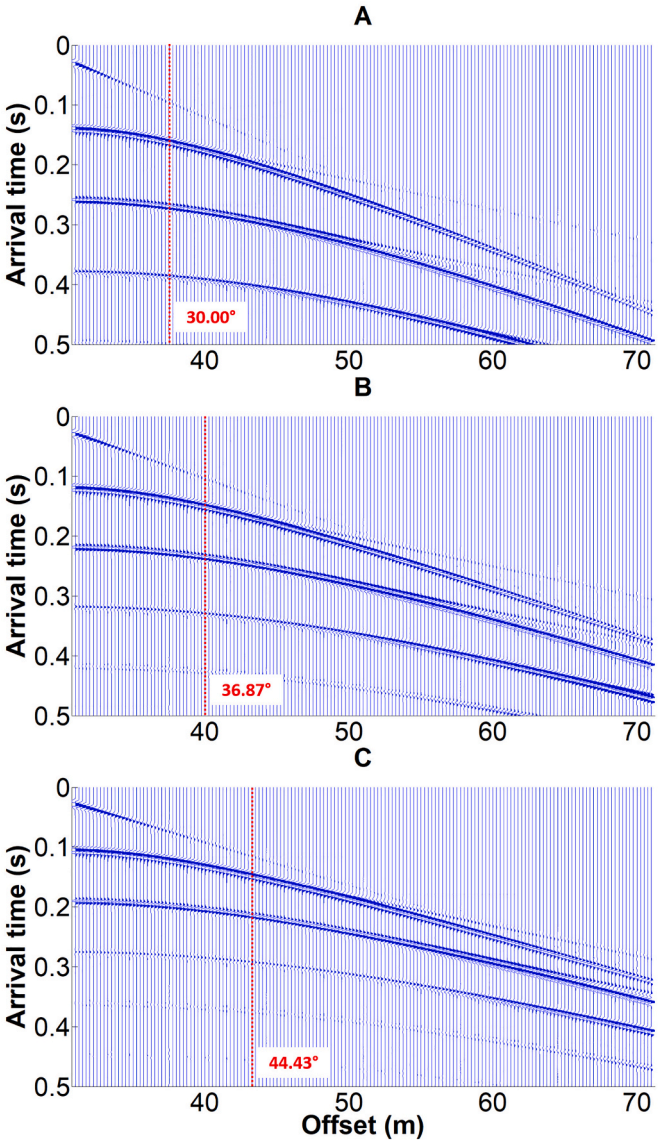

Fig. 2. Synthetic noise-free common-source gathers for the three two-layer models used in our tests. The primary reflection for the three models is characterized by the CA at (A) 30.00°, (B) 36.87°, and (C) 44.43°, respectively, as indicated by the red dotted line. (For interpretation of the references to colour in this figure legend, the reader is referred to the web version of this article.)

4. Results

4.1. Two-layer models

Our proposed approach can estimate the CA without requiring a prior velocity analysis, which allows estimation of the possible variation in the spatial location of the CA along the measurement line. We find that the CA corresponds to a specific value of the global minimum in the least-square minimization. The global minima generally vary around the CA.

We test our approach by analyzing the reflection events in three simple near-surface soil models. Each model represents a two-layer subsurface with the layer interface located at 6 m depth. The deeper layer has an S-wave velocity of 200 m/s, while the shallower layer has an S-wave velocity of 100 m/s, 120 m/s, and 140 m/s, in the first, second and third model, respectively. We simulate an S-wave survey using a finite-difference modelling scheme (Thorbecke and Draganov, 2011). For this first experiment, we use only shear-waves, because in many

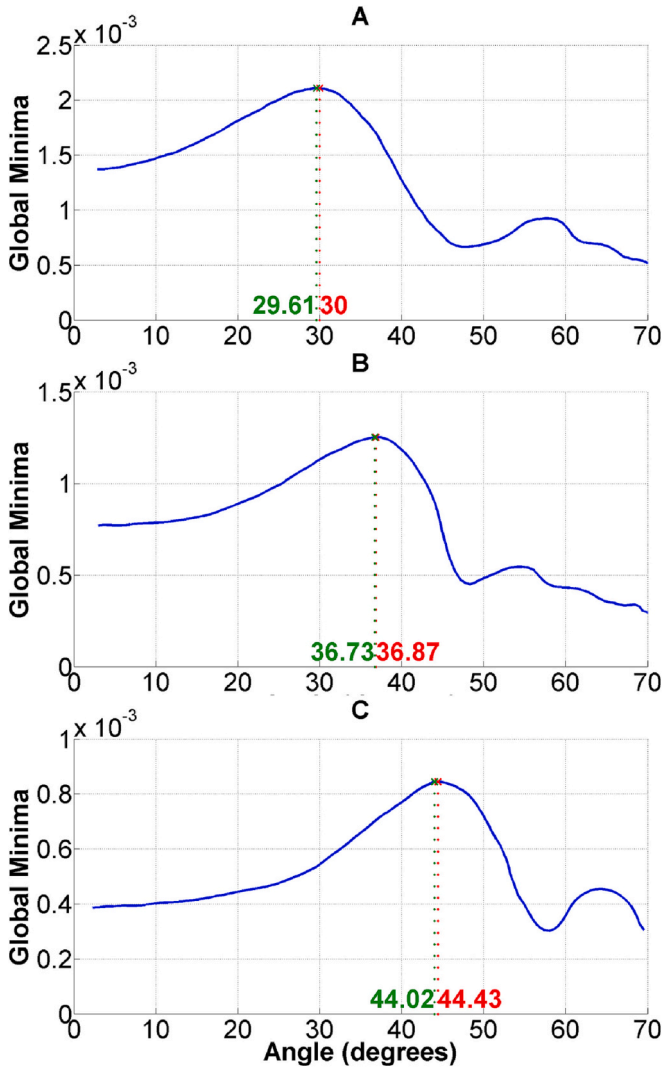

Fig. 3. Variation of the global minimum leading to an estimate of the CA (in green) for the primary reflection event in (A) Fig. 2A, (B) Fig. 2B, and (C) Fig. 2C. The correct CA is given in red. (For interpretation of the references to colour in this figure legend, the reader is referred to the web version of this article.)

near-surface surveys only S-waves are usually acquired. For each model, we pick the primary reflection from the interface of the two layers. The first model presents a CA at 30.00 degree (Fig. 2A), the second one at 36.87 degree (Fig. 2B), and the third one at 44.43 degree (Fig. 2C). Note that the refraction visually separates from the post-critical reflection at angles higher than the CA, giving a false impression that the CA exists at a lower incidence angle.

We show, in Fig. 3, the values of the global minimum for the reflection angles estimated from spectral recomposition. For the primary reflection event observed in Fig. 2A, we observe that the highest value of the global minimum is located at 29.61 degree (Fig. 3A), indicating the value of the CA. For the primary reflection events observed in Fig. 2B and C, we make the same observation — that the highest value of the global minimum corresponds to the CA at 36.73 degree (Fig. 3B) and at 44.02 degree (Fig. 3C), respectively. Because we apply our method trace-by-trace, we can stop the estimation when we detect that, beyond the highest value of the global minimum, we can recognize a steep descent of the residual (Fig. 3). For example, we can stop the estimation at about 40° in Fig. 3A, 45° in Fig. 3B, and 50° in Fig. 3C. Therefore, for estimation of the CA, our method requires relatively short offsets – offsets that allow detection of the steep descent of the residual.

Table 1
Layer parameters for the elastic four-layer model.

Layer	V_P (m/s)	V_S (m/s)	Density (kg/m3)	Layer thickness (m)
Layer 1	700	120	1000	4
Layer 2	900	170	1200	6
Layer 3	1100	240	1400	10
Layer 4	1300	330	1700	30

For the reflection event in Fig. 2A, with a CA of 30.00°, our estimated value is 29.61°. For the reflection event in Fig. 2B, with a CA of 36.87°, the estimated CA is 36.73°. For the reflection event in Fig. 2C, with a CA of 44.43°, the estimate is 44.02°. Therefore, the error is only 1.3%, 0.38%, and 0.92%, respectively, for the three cases. These results show that, on noise-free synthetic data, our proposed approach can estimate the CA quite accurately for different ranges of the CA.

4.2. Four-layer model

To test the accuracy of the Poisson's ratio estimation, we next apply our approach to a four-layer model, for which the parameters are shown in Table 1. The model is also shown in the Appendix. We simulate a combined P- and S-wave (with Ricker wavelet as source function) survey using the same finite-difference modelling scheme as before, which allows observing PP, SS, PS and SP events. The simulated common-source gather, as recorded by vertical particle-velocity receivers and a pressure source, is shown in Fig. 4A, while in Fig. 4B we illustrate the same gather after adding to it uncorrelated noise with SNR of 2. Note that the surface waves have been suppressed here through frequency-wavenumber filtering. We use both gathers to estimate the CAs of the reflections from the three interfaces and subsequently the Poisson's ratio of the top three layers.

Using the layer parameters (Table 1), we calculate the true CAs of the

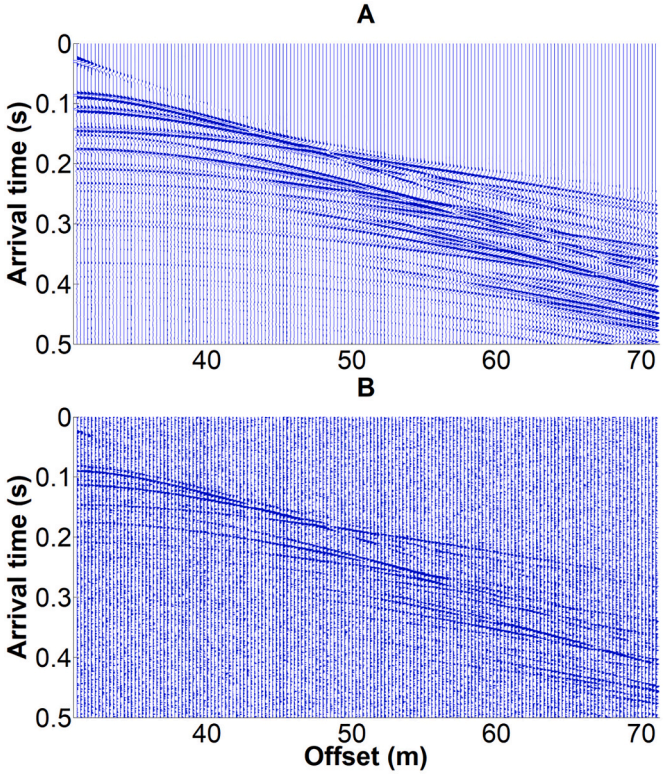

Fig. 4. Simulated common-source gather (pressure source) for the elastic four-layer model (Table 1) showing P- and S-wave reflections: (A) without noise, (B) with noise (SNR = 2).

Table 2
True CA and estimated CA for the three reflection events in the four-layer model.

Reflection events between two layers	True CA	Estimated CA for noise-free data (this research)	Error, % (noise-free data)	Estimated CA for noisy data (this research)	Error, % (noisy data)
PP 1,2	51.06°	50.45°	1.19	52.47°	2.77
PP 2,3	54.90°	54.81°	0.17	56.81°	3.47
PP 3,4	57.80°	57.65°	0.25	59.71°	3.31
SS 1,2	44.90°	44.71°	0.42	46.67°	3.94
SS 2,3	45.10°	45.03°	0.16	47.16°	4.57
SS 3,4	46.66°	45.96°	1.50	47.95°	2.77
SP 1,2	7.66°	6.67°	12.95	8.66°	13.02
SP 2,3	8.89°	8.02°	9.79	10.02°	12.71
SP 3,4	10.64°	9.74°	8.45	11.74°	10.35

PP, SS, and SP reflections for the three interfaces. Next, using the spectral-recomposition inversion as presented above, we estimate the CA (Table 2).

In Fig. 5A, B, and C, we notice that our approach estimates accurately the CA for each of the PP events. The error is less than 1.2% (Table 2).

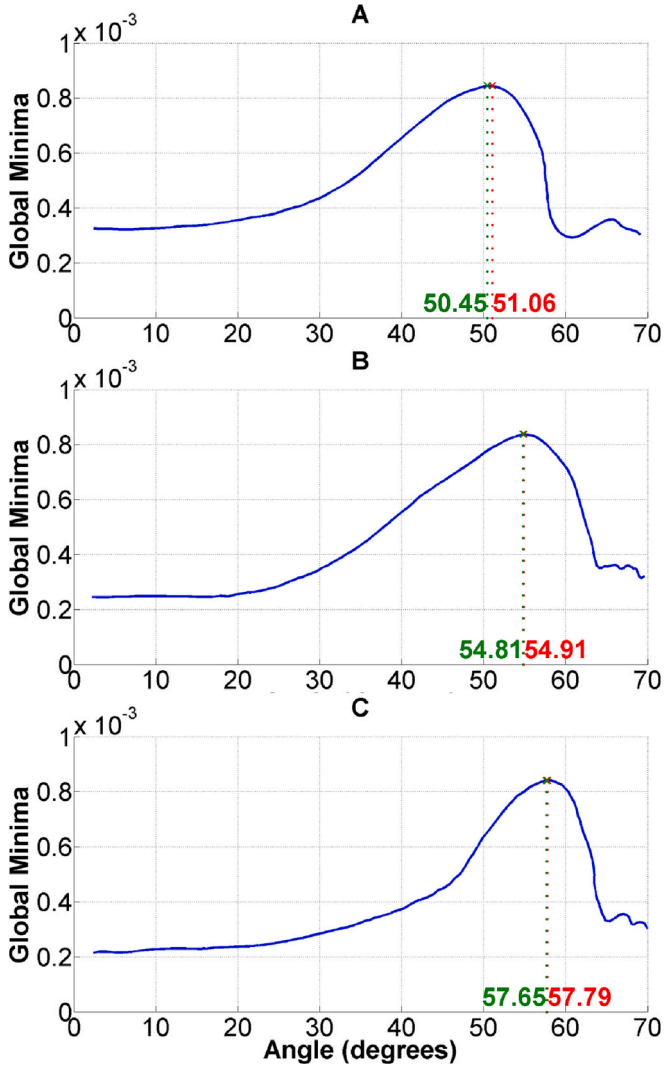

Fig. 5. Variation of the global minimum for the estimated CA (given in green) for the primary PP reflection events, in case of noise-free data (Fig. 4A), corresponding to (A) first, (B) second, and (C) third interfaces of the four-layer model. The correct value of the CA is given in red. (For interpretation of the references to colour in this figure legend, the reader is referred to the web version of this article.)

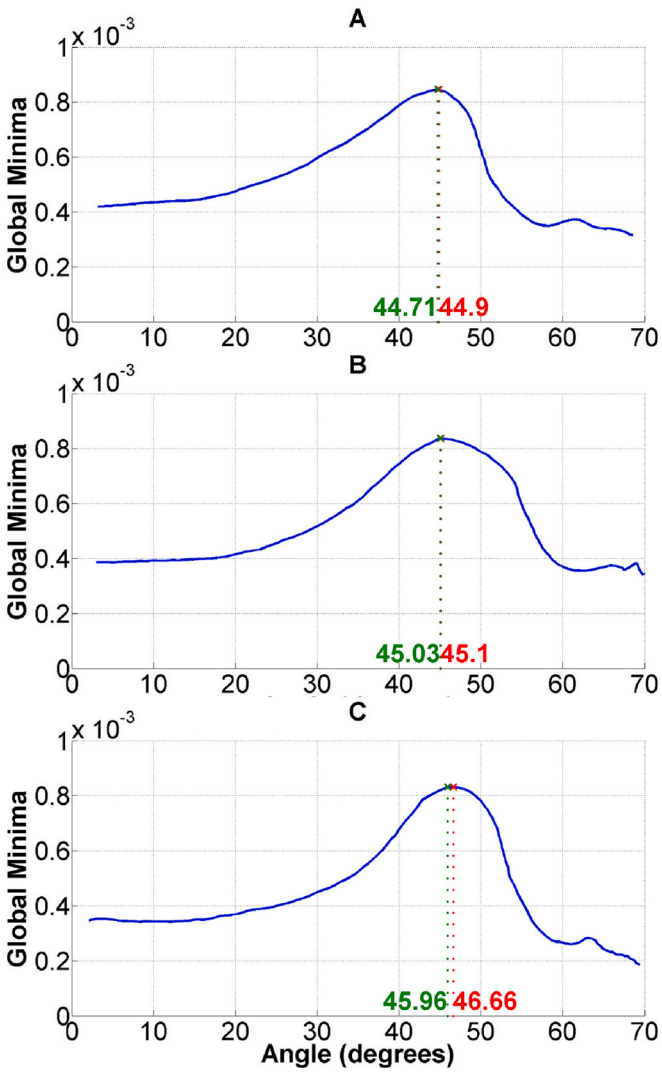

Fig. 6. Variation of the global minimum for the estimated CA (given in green) for the primary SS reflection events, in case of noise-free data (Fig. 4A), corresponding to (A) first, (B) second, and (C) third interfaces of the four-layer model. The correct value of the CA is given in red. (For interpretation of the references to colour in this figure legend, the reader is referred to the web version of this article.)

For SS reflections (Fig. 6A, B, and C), the error is found to be also less than 1.5% (Table 2). For the SP reflection events (Fig. 7A, B, and C), however, we find that the estimated CA has relatively large errors — between 8.45% and 12.95% (Table 2). Apparently, the proposed approach fails to provide accurate estimates when the CA is relatively small.

Applying our estimation procedure to a synthetic common source gather with noise (Fig. 4B), we find that, even with a SNR of 2, our approach estimates accurately the CAs of the PP events (Fig. 8A, B, and C) and of the SS events (Fig. 9A, B, and C). The error is still small - below 4.6% (Table 2). However, for the SP reflection events (Fig. 10A, B, and C), we again observe higher errors in the estimated CAs (Table 2). These results show that our approach is able to estimate in a reliable manner the position of the CA for PP, SS, and SP reflection events in different layers. It could become more difficult to estimate the CA when the SNR is much lower.

Comparing the errors in the estimates for data without and with noise (Table 2), we notice that the error in the estimated CA increases with noise much more for the PP and SS events, while it increases

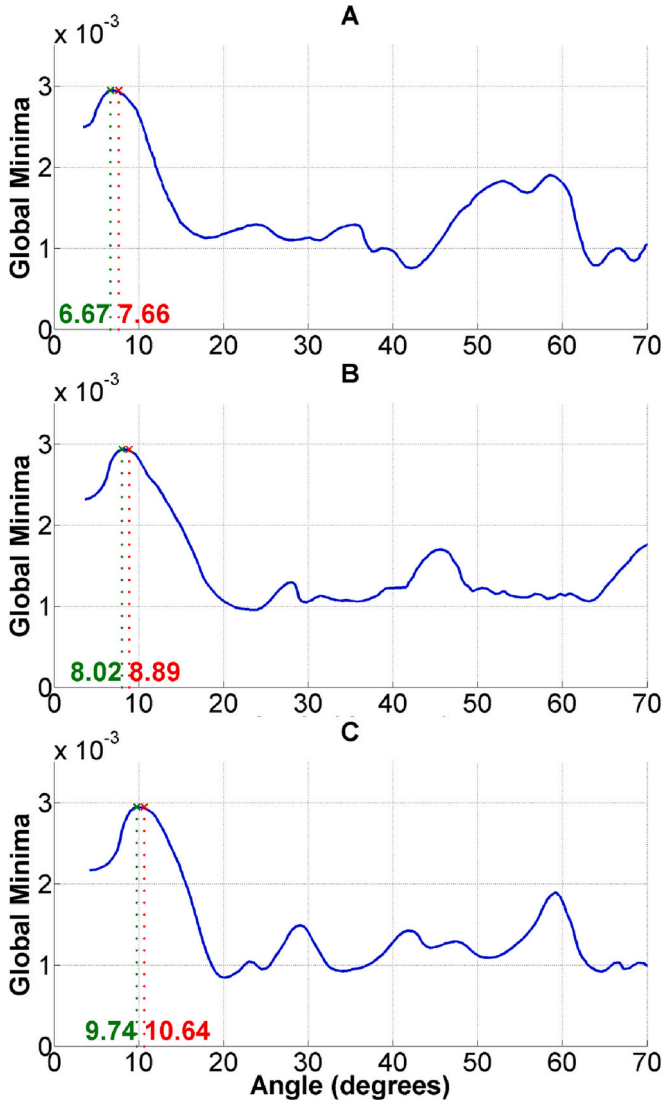

Fig. 7. Variation of the global minimum for the estimated CA (given in green) for the primary SP reflection events, in case of noise-free data (Fig. 4A), corresponding to (A) first, (B) second, and (C) third interfaces of the four-layer model. The correct value of the CA is given in red. (For interpretation of the references to colour in this figure legend, the reader is referred to the web version of this article.)

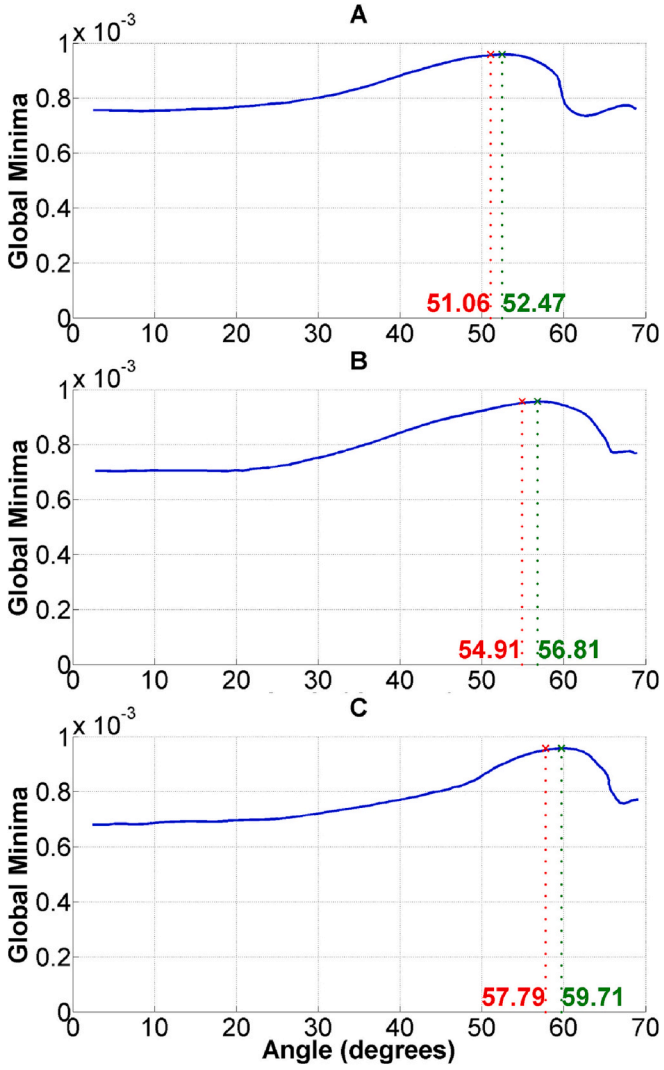

Fig. 8. Variation of the global minimum for the estimated CA (given in green) for the primary PP reflection events, in case of noisy data (Fig. 4B), corresponding to (A) first, (B) second, and (C) third interfaces of the four-layer model. The correct value of the CA is given in red. (For interpretation of the references to colour in this figure legend, the reader is referred to the web version of this article.)

relatively less for the SP events. The presence of noise influences the estimation of the CA from the variation of global minima also in another sense: in case of noise-free data, the estimated CA is always lower than the true CA, while in the presence of noise, the estimated CA is higher than the true CA for all scenarios of our tests. This suggests that the presence of noise in the data makes it more difficult for the algorithm to distinguish between the reflected and the refracted events close to the CA. For a successful CA estimation, one needs a higher incidence angle (longer offset) for clear separation of these two events.

Although the estimated CA is more erroneous for the SP events, the error in the estimated Poisson's ratio is still small – about 1% (Table 3). The same observation is also made also for data with noise (SNR of 2): the error in the estimated Poisson's ratio is still quite small. This shows that our proposed approach is robust and accurate for estimating the Poisson's ratio.

Once the Poisson's ratio for each layer is estimated, we can then estimate the velocities of each layer, in case we know the V_P of the first layer independently. Since the V_P of the first layer is usually easy to obtain (e.g., from the direct wave), we assume little error in this value. With this assumption, we estimate the V_P and V_S of each layer using our approach. The estimated values are shown in Table 4. We notice that the estimated V_P has a higher error compared to the estimated V_S. In the absence of noise, both V_P and V_S can be estimated quite accurately. In the presence of noise (SNR of 2), the estimated velocity for each layer becomes somewhat erroneous - with a very low increase in error in the estimated V_P, and a significantly higher error in the estimated V_S. Nevertheless, the velocities that we estimate following this simple approach, even in the presence of significant noise in the data, are accurate enough for use in geological characterization.

The relative errors in the estimated CAs (for both noisy data and noise-free data) are significantly higher than the errors found for Poisson's ratios. This relative insensitivity is related to the manner in which the Poisson's ratio is calculated. It happens because the ratio between values of sines of the CAs (which is equal to the V_P/V_S ratio) have small values, and they become even less significant when applied in the Poisson's ratio equation (see eqs. 12 and 13). For this reason, the relative errors in the estimated Poisson's ratio are very small in comparison to

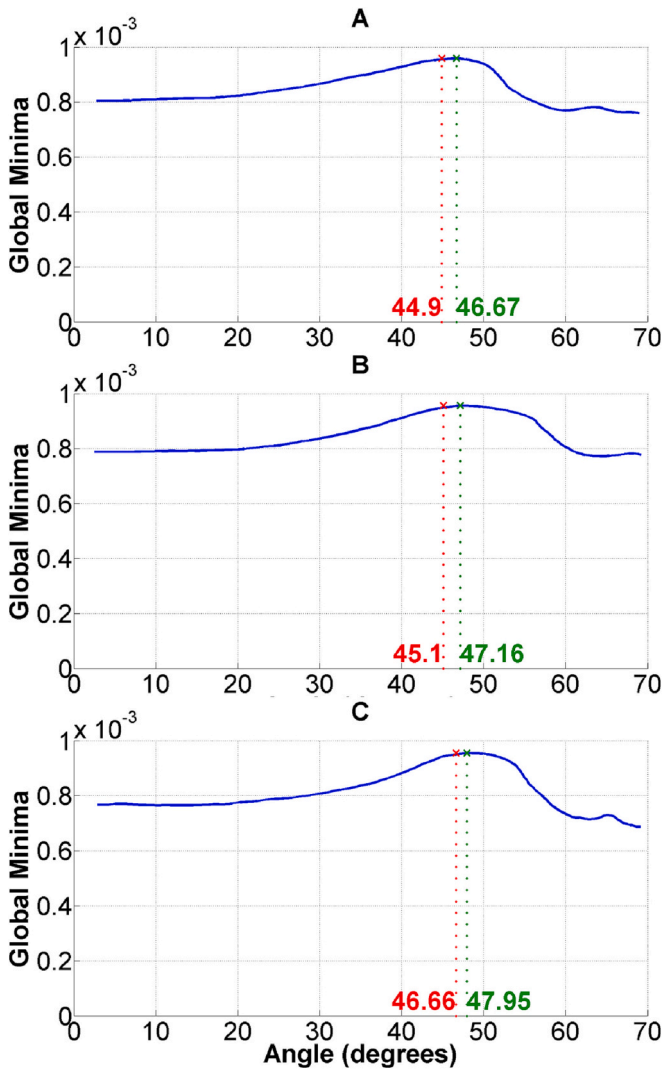

Fig. 9. Variation of the global minimum for the estimated CA (given in green) for the primary SS reflection events, in case of noisy data (Fig. 4B), corresponding to (A) first, (B) second, and (C) third interfaces of the four-layer model. The correct value of the CA is given in red. (For interpretation of the references to colour in this figure legend, the reader is referred to the web version of this article.)

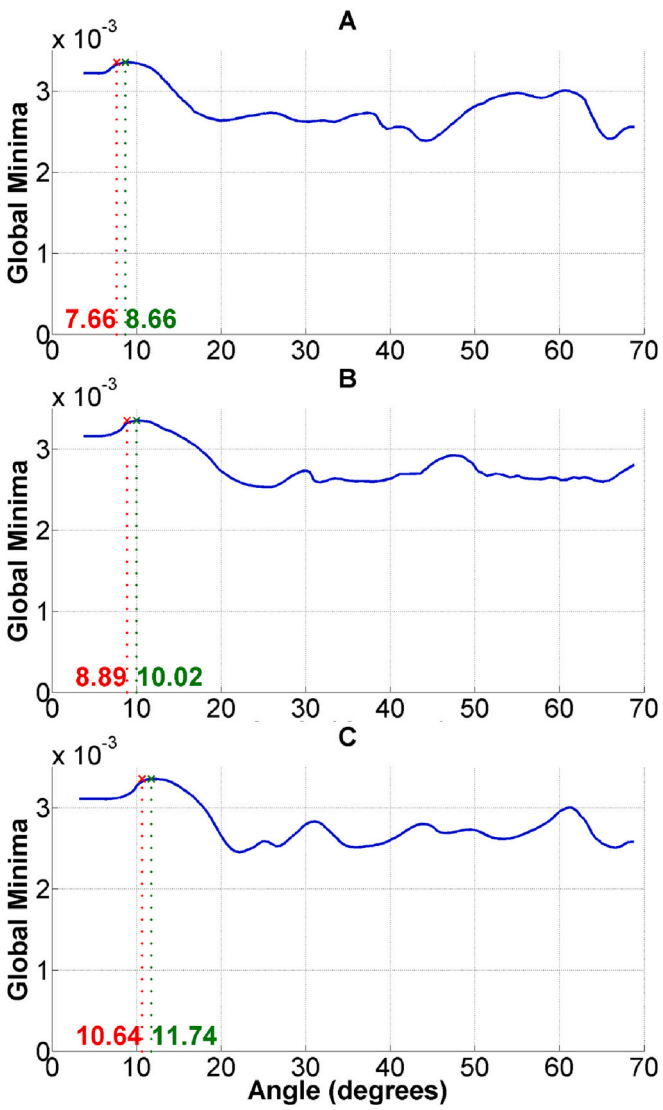

Fig. 10. Variation of the global minimum for the estimated CA (given in green) for the primary SP reflection events, in case of noisy data (Fig. 4B), corresponding to (A) first, (B) second, and (C) third interfaces of the four-layer model. The correct value of the CA is given in red. (For interpretation of the references to colour in this figure legend, the reader is referred to the web version of this article.)

errors in the respective CAs. However, the relative errors in the estimated V_P and V_S are significantly more sensitive to the error in the CAs in comparison to that in the Poisson's ratio. This is because, for the values of V_P and V_S we use, Poisson's ratio is less sensitive to changes in V_P/V_S than those in the individual values of V_P and V_S. Note that, for velocity estimation from noisy datasets, the error propagates from one layer to another during the recursion. This makes the utilization of the method less suitable when the number of layers is large.

4.3. Four-layer model inspired by field data

Again, to test the accuracy of the Poisson's ratio estimate, we apply our approach to a four-layer model inspired by field data (Gibbs et al., 1992). It represents the situation of two unsaturated layers above two saturated layers, with the water table at 13 m depth. The parameters of the model are shown in Table 5. The model is also shown in the Appendix. We simulate a P- and S-wave survey in the same manner as before, except that this time the model does not include a free surface. This means that surface waves and free-surface multiples are not modelled. For field data, this means that surface-wave suppression would have been applied, for example using data-driven interferometric surface-wave suppression (Balestrini et al., 2020), followed by surface-related multiple suppression in the raw S-wave field data (Verschuur et al., 1992; Ghose and Goudswaard, 2004). The simulated common

Table 3
True and estimated Poisson's ratio for each layer of the four-layer model.

Layer	True Poisson's ratio	Estimated Poisson's ratio (noise-free data)	Error, % (noise-free data)	Estimated Poisson's ratio (noisy data)	Error, % (noisy data)
Layer 1	0.4776	0.4828	1.08	0.4724	1.09
Layer 2	0.4728	0.4778	1.07	0.4669	1.25
Layer 3	0.4634	0.4693	1.27	0.4572	1.35

Table 4
True and estimated V_P and V_S for each layer of the four-layer model.

Layer and velocity type	True velocity (m/s)	Estimated velocity, m/s (noise-free data)	Error, % (noise-free data)	Estimated velocity, m/s (noisy data)	Error, % (noisy data)
V_P of layer 1	700	–	–	–	–
V_S of layer 1	120	119.05	0.42	132.91	10.76
V_P of layer 2	900	907.83	0.87	882.69	1.92
V_S of layer 2	170	167.85	0.09	147.23	12.29
V_P of layer 3	1100	1110.84	0.99	1054.76	4.11
V_S of layer 3	240	239.50	0.21	203.04	15.22

Table 5
Parameters of the layers in the field-inspired four-layer elastic model.

Layer	V_P (m/s)	V_S (m/s)	Density (kg/m3)	Layer thickness (m)
Layer 1	400	100	600	3
Layer 2	520	130	800	8
Layer 3	1500	250	1300	13
Layer 4	1980	330	1500	140

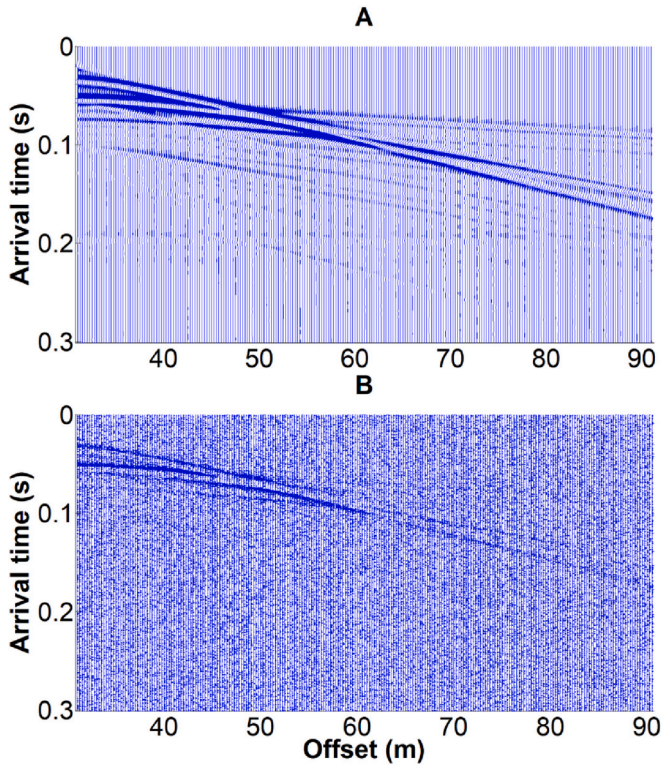

Fig. 11. Simulated common-source gather from a pressure source using the four-layer model shown in Table 5: (A) without noise, (B) with noise (SNR = 2).

source gather, as recorded by vertical-particle velocity receivers due to a pressure source, is shown in Fig. 11A, while in Fig. 11B we show the same gather after adding uncorrelated noise with SNR of 2. We use both gathers to estimate the CAs of the reflections from the three interfaces and subsequently the Poisson's ratio of the top three layers.

Using the parameters of the four layers shown in Table 5, we calculate the true CAs of the PP, SS, and SP reflections for all three

Table 6
True CA and estimated CA at the three interfaces in the four-layer model shown in Table 5.

Reflection events	True CA	Estimated CA from noise-free data (this research)	Error, % (noise-free data)	Estimated CA from noisy data (this research)	Error, % (noisy data)
PP 1,2	50.28°	49.62°	1.32	52.39°	4.19
PP 2,3	20.28°	19.71°	2.83	21.43°	5.65
PP 3,4	49.25°	48.65°	1.22	51.28°	4.12
SS 1,2	50.28°	49.71°	1.14	52.31°	4.03
SS 2,3	31.33°	30.53°	2.56	33.04°	5.45
SS 3,4	49.25°	48.27°	1.99	51.06°	3.67
SP 1,2	11.09°	10.08°	9.09	12.35°	11.39
SP 2,3	4.97°	4.26°	14.32	5.77°	16.05
SP 3,4	7.25°	6.54°	9.84	8.13°	12.08

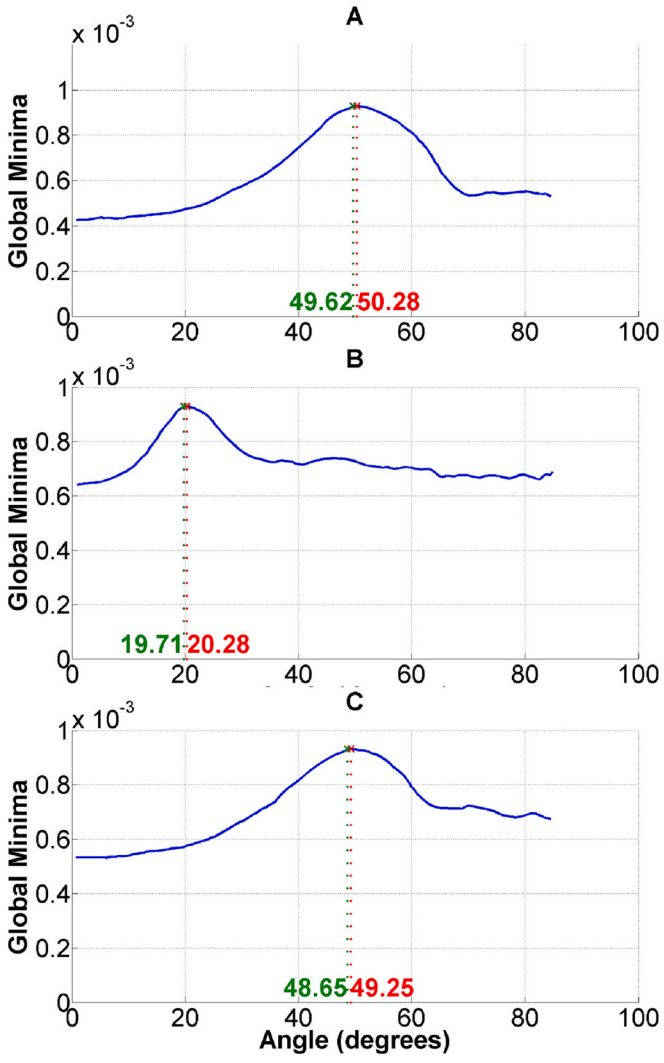

Fig. 12. Variation of the global minimum for the estimated CA (given in green) for the primary PP reflection events, in case of noise-free data (Fig. 11A), corresponding to (A) first, (B) second, and (C) third interfaces of the model in Table 5. The correct value of the CA is given in red. (For interpretation of the references to colour in this figure legend, the reader is referred to the web version of this article.)

interfaces. Next, we estimate the CA (Table 6) using the spectral-recomposition inversion developed.

In Fig. 12A, B, and C, we notice that our approach estimates accurately the CA for each of the PP events. In Figs. 12 A and 12C, the error

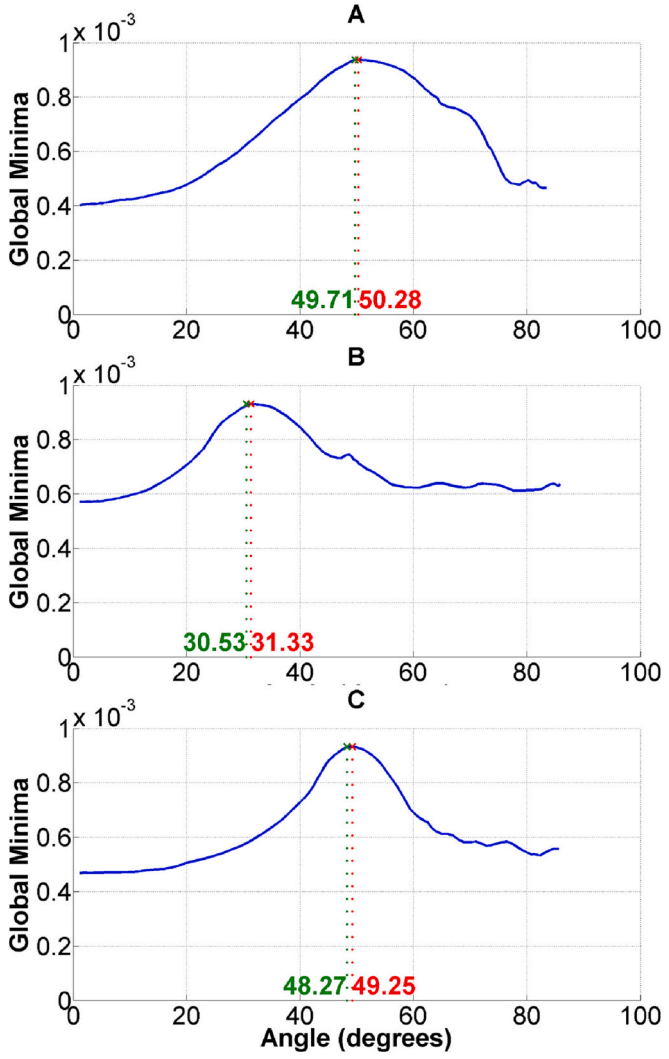

Fig. 13. Variation of the global minimum for the estimated CA (given in green) for the primary SS reflection events, in case of noise-free data (Fig. 11A), corresponding to (A) first, (B) second, and (C) third interfaces of the model in Table 5. The correct value of the CA is given in red. (For interpretation of the references to colour in this figure legend, the reader is referred to the web version of this article.)

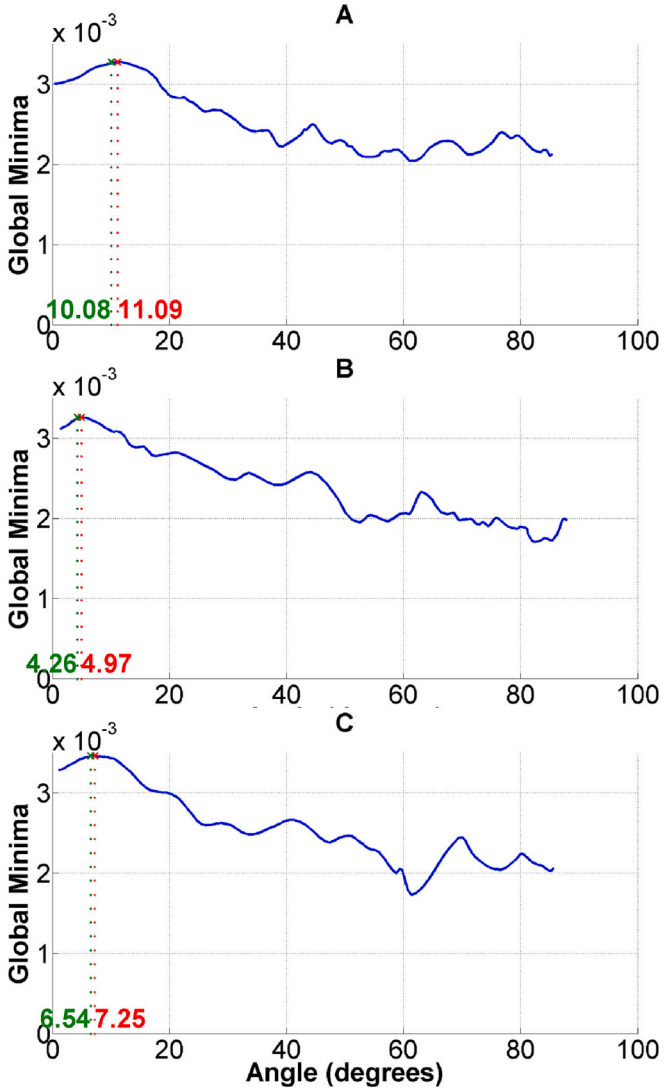

Fig. 14. Variation of the global minimum for the estimated CA (given in green) for the primary SP reflection events, in case of noise-free data (Fig. 11A), corresponding to (A) first, (B) second, and (C) third interfaces of the model in Table 5. The correct value of the CA is given in red. (For interpretation of the references to colour in this figure legend, the reader is referred to the web version of this article.)

reaches a maximum of 1.32%, while Fig. 12B shows an error of 2.83% (Table 6). For the SS reflections (Fig. 13A and C), the error reaches a maximum of 1.99% (Table 6), while for the second interface (Fig. 12B) it is 2.56%. For the SP reflection events (Fig. 14A, B, and C), however, we, again, find that the estimated CAs have a relatively larger error – a maximum of 9.84% for the first and third interfaces, while for the second interface (Fig. 14B) the error is 14.32% (Table 6). Like the previous model, the proposed approach fails to achieve a high accuracy when the CA is relatively small. We also observe that the error increases significantly at an interface when the P-wave velocity increases abruptly.

Applying our estimation procedure to the common-source gather with noise (Fig. 11B), we find that, even with a SNR of 2, our approach estimates accurately the CAs of the PP events (Fig. 15A, B, and C) and of the SS events (Fig. 16A, B, and C). The error is relatively small - below 5.7% (Table 6). However, for the SP reflection events (Fig. 17A, B, and C), we again observe relatively high errors in the estimated CAs (Table 6). These results illustrate that our approach is able to estimate reliably the position of the CAs for PP, SS, and SP reflection events also for realistic models mimicking field situations, where the P-wave velocity can experience an abrupt jump due to the presence of the water table.

Comparing the errors in the estimates for data without and with noise (Table 6), we find that the error in the estimated CA increases with noise much more for the PP and SS events than for the SP events, similar to our results for the previous model. The presence of noise again influences the estimation of the CA: in case of noise-free data, the estimated CA is always lower than the true CA, while in the presence of noise, the estimated CA is higher than the true CA for all tested scenarios.

Although the estimated CA is more erroneous for the SP events, the error in the estimated Poisson's ratio is small – less than 2.5% (Table 7). For data with noise (SNR of 2), the error in the estimated Poisson's ratio is still quite small. This confirms that our proposed method is robust and accurate for estimating Poisson's ratio.

Having obtained the Poisson's ratio for the top three layers, we can now estimate the velocities of each layer, in case we can obtain the V_P of the first layer independently. As before, we assume no error in this V_P

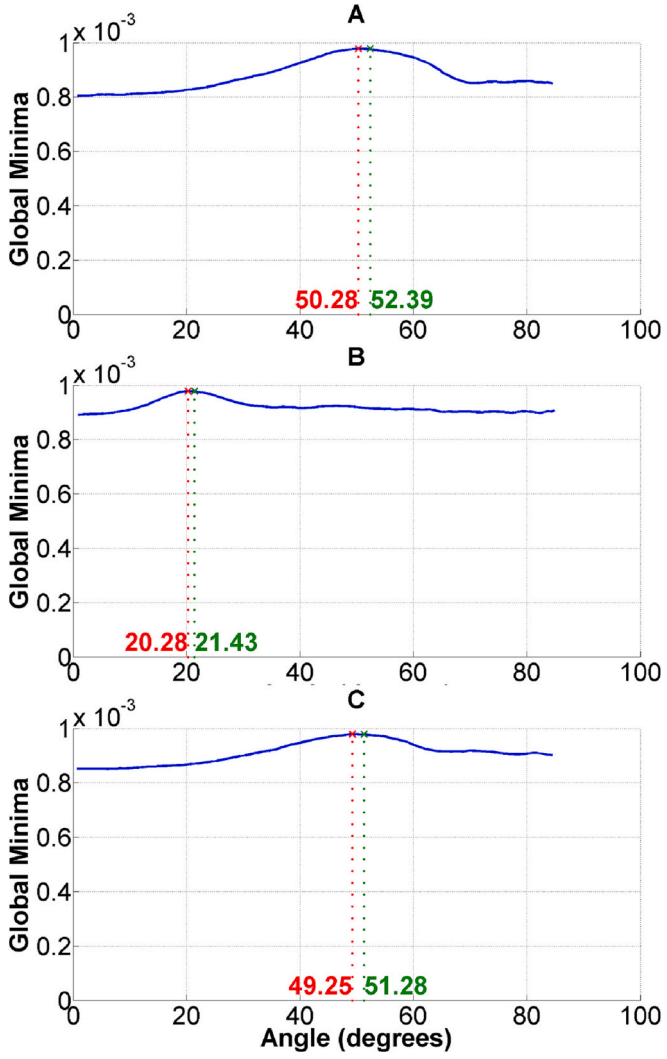

Fig. 15. Variation of the global minimum for the estimated CA (given in green) for the primary PP reflection events, in case of noisy data (Fig. 11B), corresponding to (A) first, (B) second, and (C) third interfaces of the model in Table 5. The correct value of the CA is given in red. (For interpretation of the references to colour in this figure legend, the reader is referred to the web version of this article.)

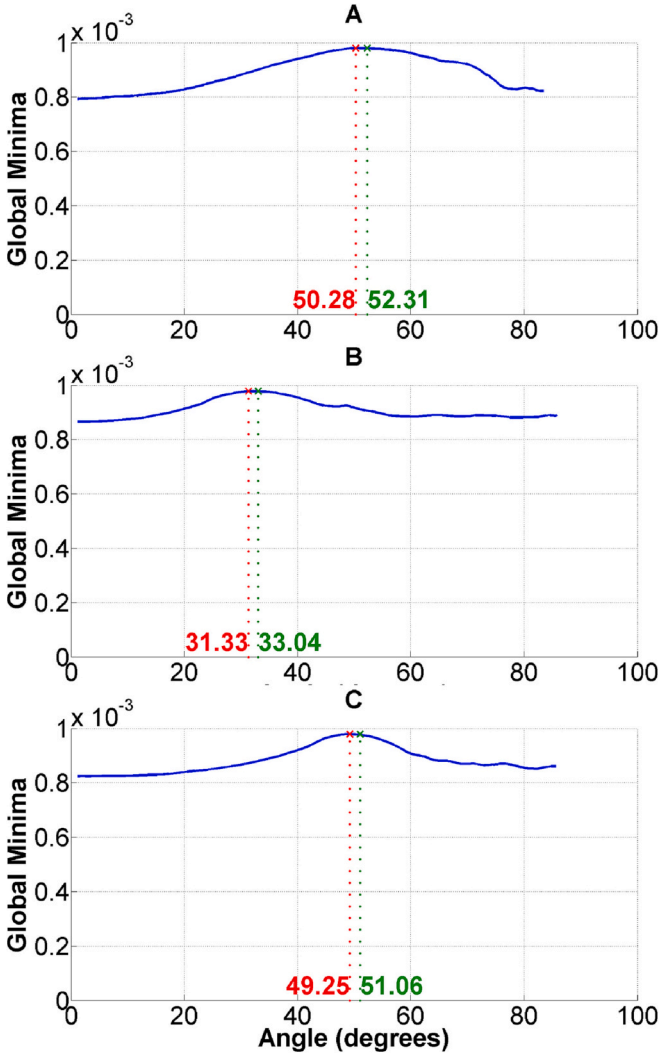

Fig. 16. Variation of the global minimum for the estimated CA (given in green) for the primary SS reflection events, in case of noisy data (Fig. 11B), corresponding to (A) first, (B) second, and (C) third interfaces of the model in Table 5. The correct value of the CA is given in red. (For interpretation of the references to colour in this figure legend, the reader is referred to the web version of this article.)

value. With this assumption, we estimate the V_P and V_S of each layer using the described approach. The estimated values are shown in Table 8. We notice that the estimated V_P has a lower error compared to the estimated V_S, which differs from the results for the previous model. For the data with noise, V_P can be estimated quite accurately, while for V_S the estimation accuracy decreases significantly but is still acceptable. In the presence of noise (SNR of 2), the estimated velocity for each layer becomes somewhat erroneous - with a very low increase in error in the estimated V_P and a significantly higher error in the estimated V_S. For the first layer, V_S obtained from the noisy data shows similar accuracy as for the noise-free data. The estimated values of V_P and V_S are accurate enough for use in geological characterization.

As we mentioned above, the small sensitivity of the Poisson's ratio to errors is also result of the field subsurface situation we use to inspire our model we use, which is characterized by high V_P/V_S ratio. For field situations with subsurface layers with low V_P/V_S ratio, for example for dry loose sand, the V_P/V_S ratio will be low, e.g., around 1.5–1.7, which would present Poisson's ratio between 0.1 and 0.24. This will result in small errors in the estimated V_P or V_S velocities producing more significant errors in the Poisson's ratio. For such field data, our method should be applied cautiously.

Another field situation important to mention is the presence of thinner layers. Such layers could generate more interference due to the arrivals from different interfaces overlaying each other. This might make it harder to identify the CA sufficiently accurately with the approach we propose.

We also performed the tests for the PP events of this data, with noise-free data and noisy data, but for a case when only offsets till 61 m are available (these results are shown in the Appendix). These results show that our approach is able to provide the proposed analyses even with short offsets.

5. Conclusions

We have proposed an alternative approach for estimating the critical angle of a reflection event by reconstructing the seismic spectrum through an inversion which is based on spectral recomposition. We calculate a spectrum that best-fits the observed spectrum. The proposed

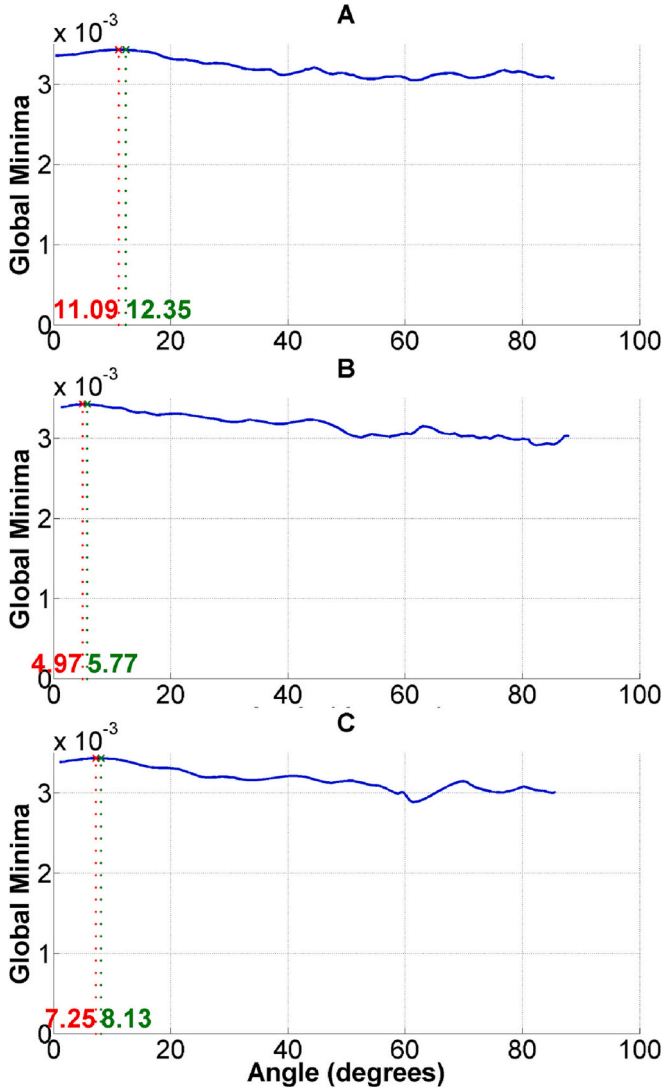

Fig. 17. Variation of the global minimum for the estimated CA (given in green) for the primary SP reflection events, in case of noisy data (Fig. 11B), corresponding to (A) first, (B) second, and (C) third interfaces of the model in Table 5. The correct value of the CA is given in red. (For interpretation of the references to colour in this figure legend, the reader is referred to the web version of this article.)

method does not require any prior velocity information. Having estimated the critical angle, the Poisson's ratio and the seismic velocities in each layer can be estimated.

In order to evaluate the capability of this approach, we have tested it on numerically modelled data of S-wave reflections from three two-layer near-surface models. We have then examined our approach on a synthetic common-source gathers containing both P- and S-wave reflections and representing two four-layer near-surface models, without and with noise (signal-to-noise ratio of 2). For the four-layer models, we have estimated the Poisson's ratio of the top three layers by first calculating the critical angle of each reflection event. Our results show that, using the new approach, it is possible to estimate the critical angle of a near-surface reflection event directly from data without performing velocity analysis, even when there is significant noise present in the data. This offers a new means to estimate quite accurately the Poisson's ratio above each of the interfaces. We have found that using the obtained Poisson's ratio information together with independently obtained value of P-wave velocity of the top layer, one can estimate the P- and S-wave velocities for each layer, without the need of conventional velocity analysis. The

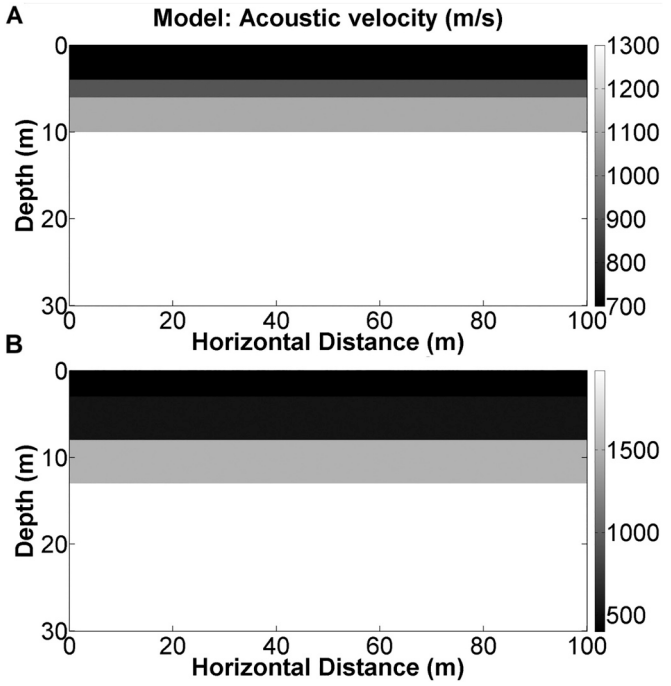

Fig. 18. (A) Four-layer velocity model shown in Table 1 and (B) four-layer model inspired by field data shown in Table 5.

Table 7
True and estimated Poisson's ratio of the top three layers for the model shown in Table 5.

Layer	True Poisson's ratio	Estimated Poisson's ratio (noise-free data)	Error, % (noise-free data)	Estimated Poisson's ratio (noisy data)	Error, % (noisy data)
Layer 1	0.4516	0.4593	1.71	0.4433	1.85
Layer 2	0.4516	0.4627	2.46	0.4410	2.35
Layer 3	0.4789	0.4825	0.76	0.4749	0.82

Table 8
True and estimated V_P and V_S for a four-layer model mimicking field situation.

Layer and velocity type	True velocity (m/s)	Estimated velocity, m/s (noise-free data)	Error, % (noise-free data)	Estimated velocity, m/s (noisy data)	Error, % (noisy data)
V_P of layer 1	400	–	–	–	–
V_S of layer 1	100	91.90	8.10	108.00	8.00
V_P of layer 2	520	525.10	0.98	504.93	2.90
V_S of layer 2	130	120.49	7.32	85.46	34.26
V_P of layer 3	1500	1556.95	3.80	1382.00	7.87
V_S of layer 3	250	237.18	5.13	156.74	37.30

method requires prior pre-processing to reduce multiples and surface waves, and time-windowing to select the target reflection events. Improvement of this method in the future should enable handling more complex wavefields and many subsurface layers.

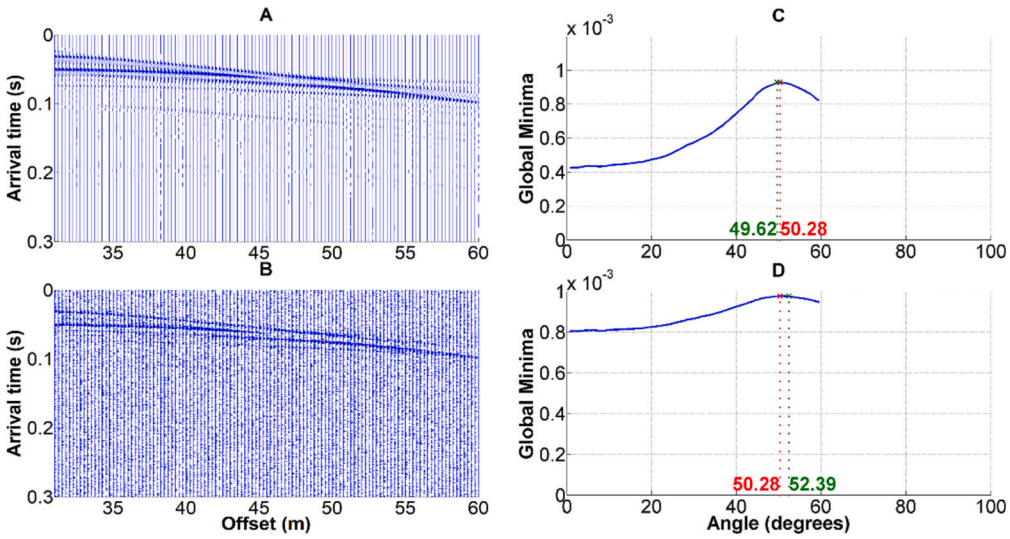

Fig. 19. Simulated common-source gather from a pressure source using the four-layer model shown in Table 5 (A) without noise and (B) with noise (SNR = 2). Variation of the global minimum for the estimated CA (given in green) for the primary PP reflection events, in case of (C) noise-free data and (D) noisy data. The correct value of the CA is given in red. (For interpretation of the references to colour in this figure legend, the reader is referred to the web version of this article.)

CRediT authorship contribution statement

Nelson Ricardo Coelho Flores Zuniga: Conceptualization, Formal analysis, Methodology, Software, Writing – original draft. **Deyan Draganov:** Data curation, Supervision, Writing – review & editing. **Ranajit Ghose:** Data curation, Supervision, Writing – review & editing.

Declaration of Competing Interest

The authors declare that they have no known competing financial interests or personal relationships that could have appeared to influence the work reported in this paper.

Data availability

In the manuscript, we inform all the parameters to generate the models and the software we used

Acknowledgements

This study was financed in parts by the Coordenação de Aperfeiçoamento de Pessoal de Nível Superior - Brasil (CAPES) - Finance Code 001 and the Conselho Nacional de Desenvolvimento Científico e Tecnológico – Brasil (CNPq).

Appendix A. Appendix

Objective function

The model is a linear combination of Ricker wavelet spectra; each spectrum is a nonlinear function that depends on two parameters. For estimating the Ricker wavelet spectra, we need the coefficients a (amplitude) and m (peak frequency). We can estimate the error using

$$r_j = d(f_j) - \sum_{i=1}^{n} a_i(m_i)\psi(m_i, f_j) \tag{14}$$

The objective junction is then formulated as least-squares estimation:

$$\min_{a,m} \| r(a,m) \|_2^2 \tag{15}$$

Example with short offsets

We show result of applying our method to the data from Table 5 but for the case when only offset till 61 m are available (Fig. 19). We notice that analyzing only few offsets beyond the CA (Fig. 19A) it is still possible to identify the position of the CA, because we can observe the decrease of the global-minima values. Looking at the case of noisy data (Fig. 19B), we see that it would demand more offsets beyond the CA, when compared to the noise-free data, to perform an accurate estimation. Nevertheless, we see that the data with offsets limited to 61 m is still sufficient to allow estimation of the CA.

References

Bachrach, R., Dvorkin, J., Nur, A., 2000. Seismic velocities and Poisson's ratio of shallow unconsolidated sands. Geophysics 65 (2), 559–564.
Balestrini, F., Draganov, D., Malehmir, A., Marsden, P., Ghose, R., 2020. Improved target illumination at Ludvika mines of Sweden through seismic-interferometric noise reduction. Geophys. Prospect. 68, 200–213.
Cai, Y., Fomel, S., Zeng, H., 2013. Automated spectral recomposition with application in stratigraphic interpretation. Interpretation 1 (1), 109–116.
Castagna, J.P., Sun, S., Siegfried, R.W., 2003. Instantaneous spectral analysis: Detection of low-frequency shadows associated with hydrocarbons. Lead. Edge 22, 120–127.
Choi, A., Zheng, Y.P., 2006. Estimation of Young's modulus and Poisson's ratio of soft tissue from indentation using two different-sized indentors: Finite element analysis of the finite deformation effect. Med. Biol. Eng. Comput. 43, 258–264.
Dunne, J., Beresford, G., 1995. A review of the τ - p transform, its implementation and its applications in seismic processing. Explor. Geophys. 26 (1), 19–36.
Ghose, R., Goudswaard, J., 2004. Integrating S-wave seismic-reflection data and cone penetration test data using a multiangle multiscale approach. Geophysics 69, 440–459.

Gibbs, J.F., Fumal, T.E., Boore, D.M., Joyner, W.B., 1992. Seismic Velocities and Geologic Logs from Borehole Measurements at Seven Strong-Motion Stations that Recorded the 1989 Loma Prieta Earthquake. U.S. Geological Survey Open-file Report 92-287. Menlo Park, California.

Huang, N.E., Shen, Z., Long, S.R., Wu, M.C., Shih, H.H., Zheng, Q., Yen, N.C., Tung, C.C., Liu, H.H., 1998. The empirical mode decomposition and the Hilbert spectrum for nonlinear and non-stationary time series analysis. In: Proceedings of the Royal Society A, 454, p. 1971.

Landro, M., Tsvankin, I., 2007. Seismic critical-angle reflectometry: a method to characterize azimuthal anisotropy? Geophysics 72 (3), D41–D50.

Law, A., Snyder, D.B., Singh, S.C., 1995. Determination of Poisson's ratio from pre-critical wide-angle seismic reflection data from the BABEL project. Geophys. J. Int. 122 (1), 16–32.

Li, Y., Zheng, X., Zhang, Y., 2011. High-frequency anomalies in carbonate reservoir characterization using spectral decomposition. Geophysics 76, V47–V57.

Nishimura, E., Kamitsuki, A., Kishimoto, Y., 1960. Some problems on Poisson's Ratio in the Earth's crust. Tellus 12 (2), 237–241.

Paskvich, S.W., 2016. Phase-Shift Measurement Analyses of Time-Lapse Multicomponent Seismic Data over a Multi-Well Hydraulic Stimulation, Wattenberg Field, Denver Basin. Master's Dissertation,. Colorado School of Mines, p. 53.

Purves, S., 2014. Phase and the Hilbert transform. Lead. Edge 33 (10), 1164–1166.

Raharjo, W., Palupi, I.R., Nurdian, S.W., Gamboro, W.S., Soesilo, J., 2016. Poisson's ratio analysis (Vp/Vs) on volcanoes and geothermal potential areas in Central Java using tomography travel time method of grid search relocation hypocenter. J. Phys. Conf. Ser. Volume 776, 8th International Conference on Physics and its Applications (ICOPIA).

Ricker, N., 1953. The form and laws off propagation of seismic wavelets. Geophysics 18, 10–40.

Roth, M., Holliger, K., Green, A.G., 1998. Guided waves in near-surface seismic surveys. Geophys. Res. Lett. 25 (7), 1071–1074.

Sil, S., Sen, M.K., 2009. Seismic critical-angle anisotropy analysis in the τ-p domain. Geophysics 74 (4), A53–A57.

Terlaky, T., Sotirov, R., 2010. Multi-Start Approach to Global Conic Optimization. ISE Archives of Working Papers.

Thorbecke, J., Draganov, D., 2011. Finite-difference modeling experiments for seismic interferometry. Geophysics 76, H1–H18.

Tomasso, M., Bouroullec, R., Pyles, D.R., 2010. The use of spectral recomposition in tailored forward seismic modeling of outcrop analogs. AAPG Bull. 94 (4), 457–474.

Verschuur, D.J., Berkhout, A.J., Wapenaar, C.P.A., 1992. Adaptive surface-related multiple elimination. Geophysics 57 (9), 1166–1177.

Yu, C., Ji, S., Li, Q., 2016. Effects of porosity on seismic velocities, elastic moduli and Poisson's ratios of solid materials and rocks. J. Rock Mech. Geotech. Eng. 8 (1), 35–49.

Zelt, C.A., Haines, S., Powers, M.H., Sheehan, J., Rohdewald, S., Link, C., Hayashi, K., Zhao, D., Zhou, H., Burton, B.L., Petersen, U.K., Bonal, N.D., Doll, W.E., 2013. Blind test of methods for obtaining 2-D near-surface seismic velocity models from first-arrival traveltimes. J. Environ. Eng. Geophys. 18 (3), 157–197.

Zhang, J.J., Bentley, L.R., 2005. Factors determining Poisson's ratio. In: CREWES Research Report, 17, pp. 1–15.

Zheng, Y.P., Choi, A.P.C., Ling, H.Y., Huang, Y.P., 2009. Simultaneous estimation of Poisson's ratio and Young's modulus using a single indentation: a finite element study. Meas. Sci. Technol. 20, 045–706.